

ARTICLE

<https://doi.org/10.1038/s42005-019-0244-3>

OPEN

# Tailoring of multi-pulse dynamics in mode-locked laser via optoacoustic manipulation of quasi-continuous-wave background

Ki Sang Lee<sup>1</sup>, Chang Kyun Ha<sup>1</sup>, Kyoung Jun Moon<sup>1</sup>, Dae Seok Han<sup>1</sup> & Myeong Soo Kang <sup>1\*</sup>

Various nonequilibrium multi-pulse states can emerge in a mode-locked laser through interactions between the quasi-continuous-wave background (qCWB) and pulses inside the laser cavity. While they have been regarded as unpredictable and hardly controllable due to the noise-like nature of qCWB, we here demonstrate that the qCWB landscape can be manipulated via optoacoustically mediated pulse-to-qCWB interactions, which alters the behaviors of multi-pulse dynamics. In this process, impulsive qCWB modulations are created at well-defined temporal locations, which act as the point emitters and attractive potentials for drifting pulse bunches and soliton rains. Hence, we can transport a single pulse bunch from a certain temporal position to another, and also make soliton rains created and collided exclusively at specific temporal locations. Our study opens up possibilities to control the nonequilibrium multi-pulse phenomena precisely in the time domain, which would offer a practical means of advanced optical information processing.

<sup>1</sup>Department of Physics, Korea Advanced Institute of Science and Technology (KAIST), 291 Daehak-ro, Yuseong-gu, Daejeon 34141, Republic of Korea.  
\*email: [mskang@kaist.ac.kr](mailto:mskang@kaist.ac.kr)

Multi-soliton dynamics has attracted great attention in a broad range of scientific disciplines, e.g., classical and quantum fluid dynamics, plasma physics, magnetism, complex networks, chemical reactions, neurosciences, and nonlinear optics<sup>1</sup>. Precise control of the behaviors of multiple solitons in the temporal or spatial domain is highly beneficial, because it offers not only an essential experimental tool for deeper understanding of multi-soliton interactions and the resulting many-body nonlinear phenomena but also a practical means of advanced information processing. In the area of nonlinear optics, mode-locked fiber lasers have been widely utilized not only as versatile sources of ultrashort optical pulses but also as fertile grounds for exploring a variety of nonlinear multi-pulse dynamics (MPD)<sup>1,2</sup>. In these systems, the interplay among the optical nonlinearities, dispersion and spectral filtering, and the inherently dissipative nature of laser cavities with the mutually counteracting gain and loss allow us to access rich MPD such as harmonic mode locking<sup>3–5</sup>, bound-state formation<sup>6–9</sup>, pulse bunching<sup>10,11</sup>, and soliton collisions<sup>12</sup>.

An important nonlinear optical effect that mediates the MPD is the long-range optoacoustic interactions among the intracavity optical pulses through the optically driven transverse acoustic resonances (ARs) in the fiber<sup>13</sup>. As a mode-locked optical pulse circulates inside the single-mode fiber laser cavity, it excites electrostrictively a sequence of AR impulses in the fiber, their temporal widths and separations being typically a few nanoseconds and a couple of tens of nanoseconds, respectively<sup>14</sup>. They create a series of impulsively time-varying refractive index modulation, which gives rise to the spectral shifts of the subsequent optical pulses. Their group velocities then change via dispersion, which yields the temporal shifts of the pulses<sup>15–17</sup>. The optoacoustic interactions in standard single-mode fiber are significant over the AR frequency range of several tens to hundreds of MHz, which in some cases acts as a limiting factor of the repetition rate of harmonic mode locking up to hundreds of MHz<sup>3–5</sup>. It has been recently demonstrated that the use of gigahertz ARs tightly confined in the micron-sized core of photonic crystal fiber can solve this issue, by stabilizing the harmonically mode-locked pulse train at the repetition rate beyond 1 GHz<sup>18–20</sup>. The formation of pulse bunches and bound pulse states via the optoacoustic inter-pulse coupling has also been investigated<sup>21–24</sup>.

Another crucial mechanism that significantly influences the MPD is the noise-like fluctuation of the quasi-continuous-wave background (qCWB) that spreads over the entire laser cavity<sup>25–30</sup>. The qCWB can be developed from the random beats of longitudinal cavity modes<sup>25</sup> or the spontaneous emission from the laser gain medium<sup>31</sup>. The qCWB fluctuation, in general, gives rise to the diffusive motion (or timing jitter) of the co-propagating mode-locked pulses<sup>26</sup>, which yields the long-range interactions among the pulses in the presence of slow gain dynamics<sup>27</sup>. Soliton rain (SR) is a representative example of the resulting nonequilibrium multi-pulse states, where soliton pulses are created spontaneously from the fluctuating qCWB and drift toward a pre-existing soliton bunch<sup>25</sup>. The qCWB fluctuation can also reportedly mediate the damped oscillation of pulse parameters and the pulse bunch formation via the long-range attractive inter-pulse interactions<sup>26,27</sup>. The effects of the qCWB have also been investigated for the cases in which continuous-wave laser light externally injected into the laser cavity plays a role of the qCWB<sup>28–30</sup>. The qCWB can then interfere with the dispersive waves shed from the soliton pulses, which leads to the drift motion of the soliton pulses. Such nonequilibrium multi-pulse phenomena, however, have been long regarded as unpredictable and hardly controllable due to their stochastic natures, and relevant previous studies thus lack a clear understanding of their origins and the underlying mechanisms.

In this paper, we address these problems by considering an intriguing situation where the inter-pulse optoacoustic interactions and the qCWB fluctuations exert a considerable impact simultaneously on the MPD in a correlated fashion. Such a possibility has not been studied yet, and there is thus still a completely unexplored regime in which the optoacoustic interactions might critically govern the behaviors of MPD. We experimentally show that the qCWB landscape can be manipulated via the optoacoustically excited ARs in the single-mode fiber laser cavity, which in turn dramatically alters the nonequilibrium MPD. In this process, a set of impulsive qCWB modulations are created in the form of intensity peaks or dips separated by the characteristic temporal periods of ARs (e.g., 21 and 33 ns for the 125- $\mu\text{m}$ -thick fiber cladding), which we can adjust potentially by changing the thickness of AR-trapping optical fiber. In particular, we demonstrate that each qCWB modulation then acts as a point emitter and an attractive potential for the drifting pulse bunches and the SR, which provides a means to control the nonequilibrium MPD precisely in the time domain in unprecedented manners. We present a physical explanation on the formation of the optoacoustic qCWB fluctuations and describe how they play a critical role in the emergence of the diverse behaviors of nonequilibrium MPD in mode-locked fiber lasers.

## Results

**Optoacoustically created impulsive qCWB modulation.** We construct a mode-locked fiber laser with unidirectional ring cavity configuration, as shown in Fig. 1, where the passive mode locking is achieved based on nonlinear polarization rotation (NPR). A 78-cm-long section of erbium-doped fiber (EDF, absorption coefficient: 110 dB m<sup>-1</sup> at 1530 nm) is used as a gain medium, which is pumped by a continuous-wave 976-nm laser diode through a wavelength division multiplexer. The total cavity length and net cavity dispersion are controlled simultaneously by adjusting the lengths of standard single-mode fiber (SMF,  $\beta_2 = -22$  ps<sup>2</sup> km<sup>-1</sup> at 1550 nm) and dispersion-compensating fiber (DCF,  $\beta_2 = +128$  ps<sup>2</sup> km<sup>-1</sup> at 1550 nm) individually. The total cavity length is in the range of 30–40 m, which corresponds to the cavity round-trip time of 150–200 ns. The laser output is obtained via a 10% tapping coupler and then observed with a 12-GHz-bandwidth photodetector and a 2.5-GHz-bandwidth oscilloscope.

The threshold pump power for mode locking varies in the range of 40–70 mW depending on the net cavity dispersion  $\beta_C$ . Above the threshold, we can generate a mode-locked pulse train and a co-propagating qCWB simultaneously, as shown in Fig. 2a, by carefully adjusting the intracavity polarization controllers (PCs). This state is readily produced at  $\beta_C < -2$  ps<sup>2</sup> km<sup>-1</sup>, i.e., unless the

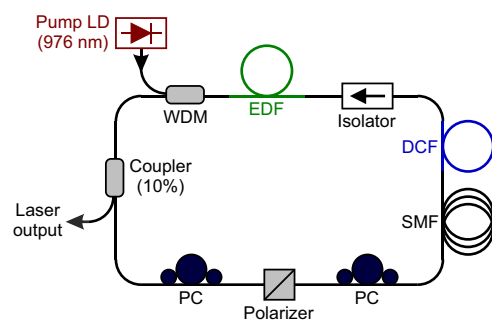


**Fig. 1** Schematic diagram of our passively mode-locked fiber laser setup. LD laser diode, WDM wavelength division multiplexer, EDF erbium-doped fiber, DCF dispersion-compensating fiber, SMF single-mode fiber, PC polarization controller

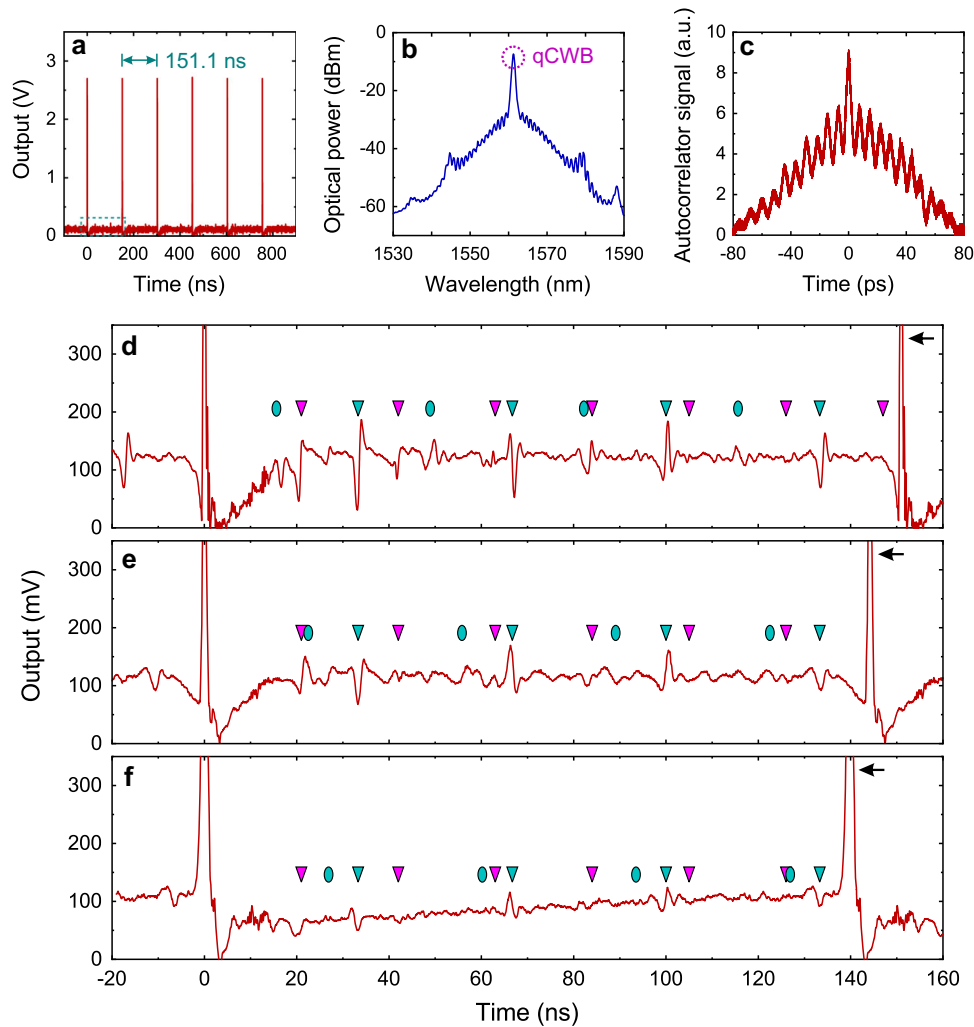


**Fig. 2** Optoacoustically induced impulsive modulation of quasi-continuous-wave background (qCWB). **a** Single-shot oscilloscope trace of the typical laser output that contains the mode-locked pulse train at the fundamental repetition rate (cavity round-trip time:  $\tau_c = 151.1$  ns) and the co-propagating qCWB. The pump power and the net cavity dispersion are set as  $P_p = 300$  mW and  $\beta_c = -4.3$  ps<sup>2</sup> km<sup>-1</sup>, respectively. **b** Optical spectrum of the laser output, where the spectral peak at 1561 nm corresponds to the qCWB, whereas the broad spectrum with the Kelly sidebands and spectral modulation to the mode-locked pulse bunches. **c** Intensity autocorrelation trace of the laser output. The almost equally spaced 21 peaks indicate that each mode-locked pulse bunch consists of 11 pulses. Their spacing of 7.4 ps is almost the same as the inverse of the spectral modulation period of 130 GHz (1.05 nm) in **b**. **d** Zoomed-in oscilloscope trace that focuses on the qCWB (corresponding to the dark cyan dashed box in **a**), which is obtained with 1000 times averaging for clear identification of the sharp intensity modulation of the qCWB. **e, f** qCWB fluctuations obtained in the same manner as **c**, but at different values of  $\tau_c$  and  $\beta_c$  by changing the length of dispersion-compensating fiber. ( $\tau_c, \beta_c$ ) = (144.2 ns,  $-8.7$  ps<sup>2</sup> km<sup>-1</sup>) for **e** and ( $\tau_c, \beta_c$ ) = (139.8 ns,  $-13.7$  ps<sup>2</sup> km<sup>-1</sup>) for **f**, while the pump power is fixed as  $P_p = 300$  mW. In **d-f**, the turquoise and magenta triangles indicate all the theoretically predicted temporal positions of AR impulses<sup>14</sup> at integer multiples of 33 and 21 ns, respectively, relative to the leftmost mode-locked pulse (at the time  $t = 0$ ). In addition, turquoise ellipses belong to the 33-ns branch of temporal locations from the mode-locked pulse in the previous round trip. The black horizontal arrows in **d-f** indicate the main mode-locked pulse in the next round trip

cavity dispersion is normal or too weakly anomalous. The laser then operates at the soliton regime, the intracavity pulse energy being set typically as  $\sim 0.1$  nJ. The existence of the qCWB is further verified by the relatively narrow spectral peak at  $\sim 1560$  nm on top of the broad pulse spectrum that exhibits the Kelly sidebands<sup>32</sup> and the spectral modulation originating from the quasi-periodic internal structure of the mode-locked pulse bunch<sup>33</sup>, as shown in Fig. 2b. At high pump powers well above the mode-locking threshold, the laser can emit a train of pulse bunches at the fundamental repetition rate<sup>11,34</sup>, its stable formation being supported by the intracavity third-order dispersion<sup>35</sup>. Whereas in the oscilloscope traces each bunch is not fully resolved and appears as a single pulse because of the insufficient bandwidth of the oscilloscope, we can observe the fully resolved quasi-periodic

internal structure of the bunch via intensity autocorrelation measurement<sup>33</sup>, as shown in Fig. 2c. The temporal spacing between the adjacent picosecond pulses in a bunch is determined as 7.4 ps, which is almost the same as the inverse of spectral modulation period in the optical pulse spectrum of 130 GHz (1.05 nm) in Fig. 2b. Furthermore, we can also accurately identify the total number of pulses inside each bunch from the intensity autocorrelation trace, which is generally around 10 depending on the pump power and the state of intracavity PCs (i.e., intracavity nonlinear loss). We note that the measured bunch power (e.g.,  $\sim 0.5$  mW for Fig. 2a–d) tends to increase with the number of pulses in a bunch, but its significant dependence on the state of intracavity PCs hinders the accurate determination of the number of pulses solely from the bunch power.

Focusing on the qCWB part (dark cyan dashed box in Fig. 2a), we observe sharp intensity modulation of the qCWB, as shown in Fig. 2d. The qCWB modulation peaks at almost regularly spaced temporal locations, and their spacing measured as 33 or 21 ns is interestingly close to the temporal period of the previously reported optoacoustic impulse response to a single optical pulse via electrostriction in a 125- $\mu\text{m}$ -thick optical fiber<sup>14</sup>. We compare the temporal positions of experimentally observed qCWB peaks or dips with those of the theoretically predicted optoacoustically induced AR impulses (indicated by turquoise and magenta markers in Fig. 2d–f)<sup>14</sup>, which reveals that the qCWB peaks appear close to the locations of AR impulses. These peaks are a part of the qCWB rather than that of the mode-locked pulse train, which is seen from the fact that they can be observed only when the qCWB exists. The most marked group of qCWB peaks that appear integer multiples of 33 ns after a mode-locked pulse (turquoise triangles in Fig. 2d–f) can be produced by the torsional–radial  $\text{TR}_{2m}$  ARs in the torsional branch. Another group of the relatively weak qCWB peaks appearing at integer multiples of 21 ns (magenta triangles in Fig. 2d–f) is contributed primarily by the  $\text{TR}_{2m}$  ARs in the radial branch. While the radial  $\text{R}_{0m}$  ARs are also known to generate a series of AR impulses at integer multiples of 21 ns<sup>14</sup>, we experimentally verify that the qCWB exhibits the features of the  $\text{TR}_{2m}$  ARs only rather than those of the  $\text{R}_{0m}$  ones, by investigating the electrical spectrum of the pure qCWB state (see Supplementary Note 1 for more detail). There are also qCWB peaks at 16, 49, 82, and 116 ns from the mode-locked pulse (turquoise ellipses, most apparent in Fig. 2d), which originate from the optoacoustic response to the mode-locked pulse in the previous round trip. From the cavity round-trip time of 151 ns, their actual temporal positions are determined as 167, 200, 233, and 267 ns, respectively, which belong to the 33-ns  $\text{TR}_{2m}$  branch. Such sharp qCWB modulations can be observed over wide ranges of cavity parameters such as the cavity length, cavity dispersion, and pump power, with careful adjustment of the intracavity PCs. We check that the peak intervals of 33 and 21 ns are almost unaffected by the change in all these cavity parameters, which further confirms that they are relevant to the AR properties rather than the optical ones, although the detailed pattern of the qCWB modulation may vary. In addition, we do not see any apparent correlation between the optical spectrum of the laser output and the features of the qCWB modulation in the time domain. We note that we can readily observe the dominant qCWB peaks at integer multiples of 33 ns for  $\beta_C < -2 \text{ ps}^2 \text{ km}^{-1}$ . In particular, at the relatively weak anomalous regime of  $-6 \text{ ps}^2 \text{ km}^{-1} < \beta_C < -2 \text{ ps}^2 \text{ km}^{-1}$ , only the 33-ns branch of qCWB peaks is predominantly observed, whereas the 21-ns branch is rarely seen. Although the 21-ns branch becomes apparent at the cavity dispersion more anomalous beyond  $-6 \text{ ps}^2 \text{ km}^{-1}$ , we do not investigate it in detail, as it does not affect the MPD significantly in our case.

One might think that the AR-induced phase modulation<sup>36–39</sup> could give rise to the qCWB peaks through interferences. The 21-ns  $\text{R}_{0m}$  AR branch of qCWB fluctuations should be then predominant compared with the 33-ns one, as the magnitude of the optoacoustic impulse response mediated by the  $\text{R}_{0m}$  ARs is stronger than that by the  $\text{TR}_{2m}$  ones approximately by a factor of 10 or larger<sup>14</sup>. In our case, however, the 33-ns  $\text{TR}_{2m}$  branch is stronger and appears more readily, whereas the 21-ns one is relatively weak and observed intermittently. This strong contradiction rejects the possibility of the AR-induced phase modulation as the primary origin of the qCWB peaks. On the other hand, it is known that the  $\text{TR}_{2m}$  ARs can also yield the polarization modulation through depolarized scattering<sup>13</sup>. In our NPR-based mode-locked fiber laser, the intracavity polarizer can transform the polarization modulation into the intensity modulation, which results in the qCWB modulation.

To verify and further understand the role of the TR–AR-induced polarization coupling and intracavity polarizer in the formation of the qCWB modulation, we construct another mode-locked fiber laser that is very similar to Fig. 1 but incorporates a semiconductor saturable absorber mirror (SESAM) as a mode locker and excludes the polarizer. The SESAM has a relaxation time of 2 ps, and its small-signal absorbance and modulation depth are 12 and 7%, respectively, which are appropriate for the simultaneous generation of the mode-locked pulses and qCWB. We can reproduce a set of impulsive qCWB fluctuations in this case. In contrast to the case of the NPR-based mode locking, however, it turns out that they appear mostly at integer multiples of 21 ns at any cavity parameter, whereas their creation at integer multiples of 33 ns is hardly observed, as shown in Fig. 3a. This result points out that the intracavity polarizer plays a critical role in the formation of the optoacoustic qCWB fluctuations spaced by 33 ns. For further comparison to figure out the role of the intracavity polarizer, we also generate a continuous-wave output from the laser after excluding the intracavity polarizer and the SESAM to suppress any type of passive mode locking and measure the electrical spectrum of the laser output. Unlike the electrical spectrum in Supplementary Fig. 10, we observe a group of spectral peaks at the integer multiples of either 30 (Fig. 3b) or 47 MHz (Fig. 3c), depending on the state of intracavity PCs and the pump power. These two characteristic peak-to-peak separations can also appear simultaneously (Fig. 3d). The frequency spacings of 47 and 30 MHz correspond to the modulation periods of 21 and 33 ns, respectively, which indicates that in the absence of the intracavity polarizer, both the radial and the torsional branches can reveal themselves in the qCWB.

### Tailoring of MPD via optoacoustically manipulated qCWB.

We observe various types of MPD phenomena that are mediated by the TR–AR-induced optoacoustic qCWB fluctuations. As we will discuss later, the qCWB peaks can act as attractive potentials for optical pulses in the anomalous dispersion regime. First, it is then possible to trap a single pulse (or pulse bunch) at one qCWB peak and transport it to another, as described in Fig. 4a–c (also see Supplementary Fig. 1 and Supplementary Movie 1). After generating a train of mode-locked pulses and the qCWB simultaneously, we can produce additionally a relatively small pulse at one optoacoustic qCWB peak (located at  $3\tau_T = 100$  ns from the main mode-locked pulse in the case of Fig. 4a), by carefully adjusting the intracavity PCs. We can then perturb the trapped small pulse to release it from the qCWB peak and drift, as shown in Fig. 4b, by slightly changing the state of the intracavity PCs. We experimentally observe that the drift speed tends to get smaller as the magnitude of the net cavity dispersion  $|\beta_C|$  decreases. We can understand this tendency from the fact that the drifting pulse has a slightly different center wavelength from the main mode-locked pulses<sup>40</sup>, and a larger value of  $|\beta_C|$  yields a greater difference of group velocity between them, i.e., a higher drift speed. When the drift is sufficiently slow, the small pulse can be captured at the next optoacoustic qCWB peak (located at  $4\tau_T = 133$  ns in the case of Fig. 4c). These observations indicate a new possibility that we can make use of the optoacoustic qCWB fluctuations to control the motion of small pulses on the qCWB landscape precisely in the time domain, in the way of storing and transferring them at specific temporal positions that we target.

We can also generate several small drifting pulses that are distributed initially over the entire qCWB landscape, as shown in Fig. 4d, by adjusting the intracavity PCs at the pump powers well above the mode-locking threshold. Although the pulses drift seemingly in a random way at the beginning, their motions eventually stop at the series of qCWB peaks or the main pulses to

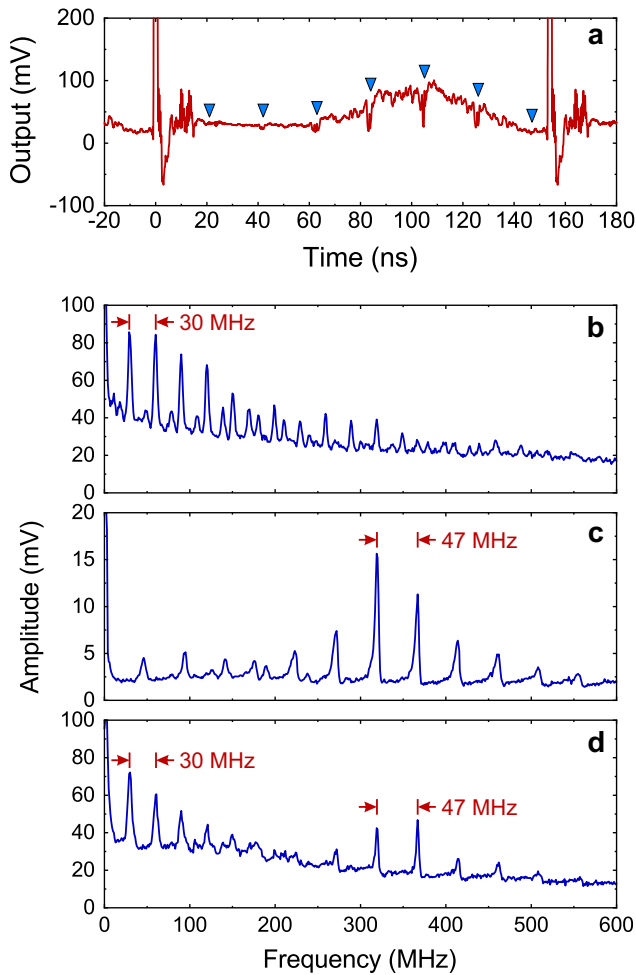


**Fig. 3** Optoacoustically induced quasi-continuous-wave background (qCWB) modulations from the laser excluding the intracavity polarizer. **a** Typical averaged oscilloscope trace that is zoomed in around the impulsive qCWB modulations when the laser is passively mode-locked by using a semiconductor saturable absorber mirror (SESAM) as a saturable absorber. The pump power is set as  $P_p = 300$  mW. Blue triangles indicate the theoretically predicted temporal locations of integer multiples of 21 ns relative to the leftmost mode-locked pulse (at the time  $t = 0$ ). **b-d** Electrical spectra of the continuous-wave output from the laser in which passive mode locking is suppressed by removing both the intracavity polarizer and the SESAM. In **b**, the spectrum exhibits several peaks at integer multiples of 30 MHz. In **c**, the spectrum displays several peaks at integer multiples of 47 MHz. In **d**, the spectrum contains both the 30- and the 47-MHz-branch ones. The pump powers are  $P_p = 80$  mW for **c** and  $P_p = 400$  mW for **b** and **d**. The resolution bandwidth of the radio-frequency spectrum analyzer is fixed as 2 MHz for **b-d**

yield a regularly spaced pulse pattern, as shown in two examples of steady states of Fig. 4e, f (also see Supplementary Fig. 2 and Supplementary Movie 2 for the entire organization process that is obtained at  $\beta_C = -5.2$  ps<sup>2</sup> km<sup>-1</sup>). This type of pulse pattern formation is observed more readily when the drift of small pulses is sufficiently slow, and the optoacoustic qCWB peaks are more apparent. This condition is achieved when the net cavity dispersion  $\beta_C$  is slightly anomalous but not too small so as to keep the simultaneous generation of the main mode-locked pulses and the qCWB, typically within the range of  $-7$  to  $-2$  ps<sup>2</sup> km<sup>-1</sup>. In some cases, a part of 33-ns-branch qCWB peaks may diminish, where the drifting pulses can be hardly trapped. For instance, in the case of Supplementary Fig. 2 and Supplementary Movie 2, the

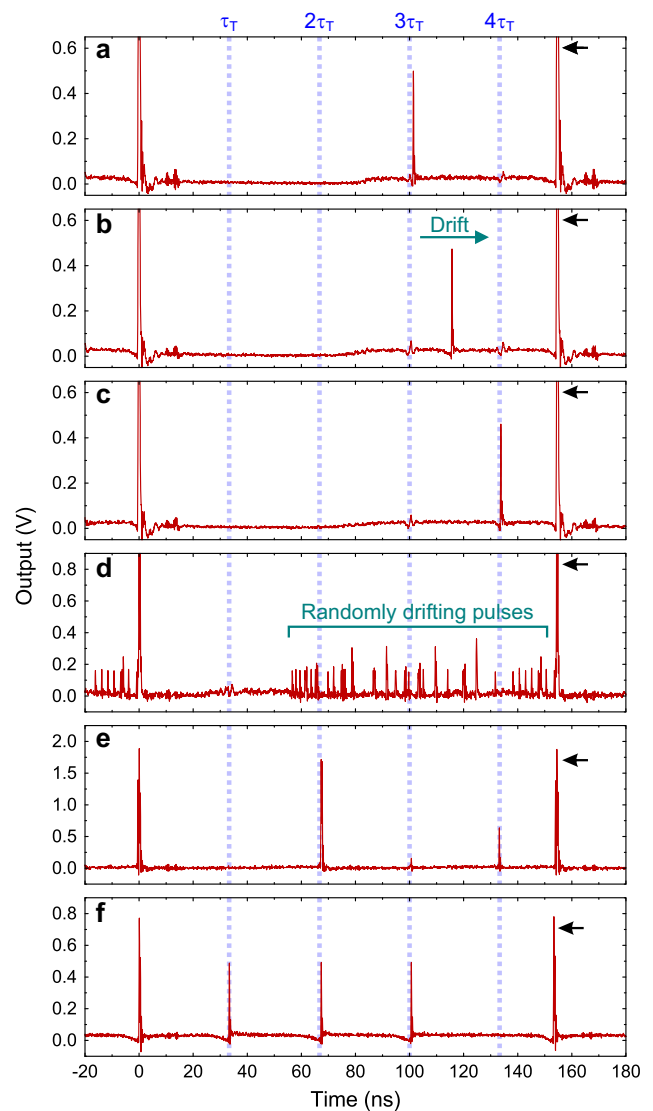


**Fig. 4** Oscilloscope traces that display dynamic multi-pulse phenomena strongly affected by the optoacoustic quasi-continuous-wave background (qCWB) peaks. **a-c** Transport of a single pulse bunch between two neighboring qCWB peaks at  $3\tau_T = 100$  ns and  $4\tau_T = 133$  ns. The cavity parameters are  $\tau_C = 154.6$  ns,  $\beta_C = -4.7$  ps<sup>2</sup> km<sup>-1</sup>, and  $P_p = 300$  mW. In **a**, a small pulse bunch is initially trapped at  $3\tau_T = 100$  ns. In **b**, when we perturb this state by slightly changing the intracavity polarization controllers (PCs), the pulse bunch starts to drift toward the next main mode-locked pulse at  $\tau_C = 154.6$  ns (indicated by the black arrow). The drift speed is determined as 16 fs km<sup>-1</sup>. Note the maintenance of both the qCWB peaks at  $3\tau_T = 100$  ns and  $4\tau_T = 133$  ns. In **c**, the drifting pulse bunch is captured and stably held at the next optoacoustic qCWB peak at  $4\tau_T = 133$  ns. **d** Typical multi-pulse state in which a large number of small pulses drift randomly over the qCWB landscape. **e, f** Two examples of final steady states of **d**, where the set of small drifting pulses in **d** is organized eventually into multiple pulse bunches trapped at the optoacoustic qCWB peaks, which form regularly spaced pulse patterns with the spacing of  $\tau_T = 33$  ns

qCWB peak is not apparent at  $\tau_T = 33$  ns, and as a result the drifting pulses are not captured there. We note that in the presence of the qCWB dips that mostly appear at the relatively more anomalous regime (i.e., at larger values of  $|\beta_C|$ ), not to be presented here in detail, we usually observe the chaotic drift of pulses that are created spontaneously from the qCWB in an

uncontrollable manner. In addition, in the case of SESAM-based mode-locked lasers where the qCWB contains only intensity dips at integer multiples of 21 ns (Fig. 3a), we normally see irregularly repeated creation and disappearance of noisy pulses at arbitrary temporal locations, and thus it is difficult to find any apparent influence of the optoacoustic qCWB dips on MPD.

The formation of the attractive potentials at which the drifting pulses are eventually captured can be contributed in general by two mechanisms. First, the optical pulses nearby the optoacoustically driven acoustic impulses experience frequency shifts through the sharp photoelastic index fluctuations, which then act as the attractive potentials under the anomalous dispersion. While this type of long-range pulse-to-pulse interactions has been recently investigated in the context of temporal cavity solitons<sup>17,22</sup>, the previous works considered only the radial  $R_{0m}$  ARs with the fully scalar analysis. On the other hand, the  $TR_{2m}$  ARs that play a predominant role in our case yield much weaker photoelastic index changes by a factor of 1/10 or less compared with the radial ARs<sup>14</sup>. Hence, if the photoelastic frequency shift created by the acoustic impulses is the dominant mechanism of the pulse trapping, it would take place much more readily at the temporal locations of the integer multiples of 21 ns that is the characteristic of the  $R_{0m}$  ARs rather than of the integer multiples of 33 ns. Another possible physical mechanism is the interaction between the drifting pulses and the intensity peaks on the qCWB via the cross-phase modulation (XPM). The drifting pulses experience larger refractive indices at the qCWB peaks through the XPM compared with outside of the qCWB peaks, so the pulses can be trapped at the qCWB peaks. We can validate the trapping of drifting pulses at the optoacoustic qCWB peaks via simple theoretical estimation of the frequency shift, i.e., the temporal rate of phase shift, arising from each of the two mechanisms. In our experimental conditions at the nominal pump power of 300 mW, the power modulation at the optoacoustic qCWB peak is measured as typically  $\sim 30$  mW (Fig. 4b). The XPM-induced phase shift at the qCWB peak per unit propagation length in our cavity (net cavity nonlinearity:  $\gamma_C = 2.0 \text{ W}^{-1} \text{ km}^{-1}$ ) is then  $0.12 \text{ rad km}^{-1}$ . On the other hand, the TR-AR-induced photoelastic phase shift per unit propagation length is estimated below  $9 \text{ mrad km}^{-1}$  for the measured intracavity energy of  $\sim 1 \text{ nJ}$  of each mode-locked pulse bunch<sup>14,37</sup>. In our case, therefore, the trapping of drifting pulses is mainly contributed by the XPM-induced pulse frequency shift rather than the photoelastic counterpart, and we verify that the resulting amount of refractive index modulation is indeed sufficient for the capturing of drifting pulses (see Supplementary Note 2 for more detail).

We also observe another type of interesting MPD phenomena, where a variety of SR dynamics emerges as the TR-AR-induced optoacoustic qCWB fluctuations that radically alter the SR. The SR is formed when the pulse-like fluctuations created on the qCWB from the random beats of longitudinal laser modes are developed into soliton pulses through instantaneously saturated losses<sup>25</sup>. Hence, the SR can be produced in principle at almost arbitrary temporal locations on the qCWB landscape, and the resulting drifting pulses are absorbed eventually at the main mode-locked pulses. In strong contrast to the conventional SR, in our case, the optoacoustic qCWB peaks act as the discrete “point sources” of the SR, i.e., the SR is emitted from the qCWB peaks only, whereas its generation from the other temporal positions is highly suppressed, as shown in Fig. 5a, b (see Supplementary Figs. 3 and 4 and Supplementary Movies 3 and 4, which display the SRs generated at the qCWB peaks at  $3\tau_T = 100 \text{ ns}$  and  $4\tau_T = 133 \text{ ns}$ , respectively, from the main mode-locked pulse). Furthermore, we can make the SRs produced simultaneously at multiple qCWB peaks, as shown in Fig. 5c (also see Supplementary Fig. 5 and Supplementary Movie 5 that show SR generation simultaneously from the two qCWB peaks at  $3\tau_T = 100 \text{ ns}$  and  $4\tau_T = 133 \text{ ns}$ ). The

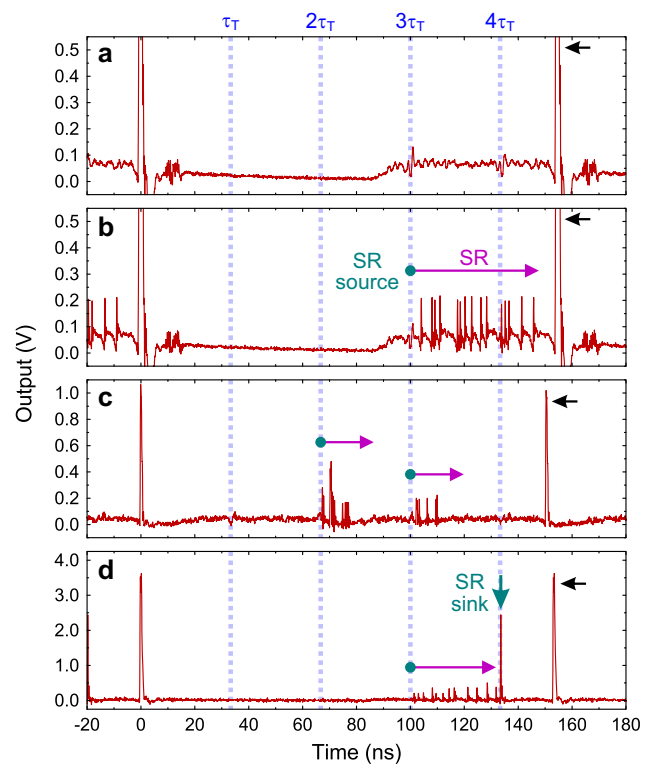


**Fig. 5** Oscilloscope traces that show soliton rain (SR) states strongly affected by the optoacoustic quasi-continuous-wave background (qCWB) peaks. **a** qCWB exhibiting optoacoustically induced sharp fluctuations at  $3\tau_T = 100 \text{ ns}$  and  $4\tau_T = 133 \text{ ns}$ . The cavity parameters are the same as in Fig. 4a–c, i.e.,  $\tau_C = 154.6 \text{ ns}$  and  $\beta_C = -4.7 \text{ ps}^2 \text{ km}^{-1}$ , but the pump power is increased to  $P_p = 570 \text{ mW}$ . **b** SR is emitted exclusively from a single optoacoustic qCWB peak at  $3\tau_T = 100 \text{ ns}$ , whereas the SR generation from the other arbitrary temporal positions is highly suppressed. This state is obtained by slightly changing the state of the intracavity PCs from **a**. The SR collides eventually at the next main mode-locked pulse at  $\tau_C = 154.6 \text{ ns}$  (indicated by the black arrow). **c** The SR can also be generated at multiple optoacoustic qCWB peaks at the same time. **d** When the drift speed of the SR is sufficiently low, it can collide at the next optoacoustic qCWB peak at  $4\tau_T = 133 \text{ ns}$ , rather than the main mode-locked pulse. The energy carried by the SR is then accumulated at the “SR sink”, which yields the growing pulse bunch trapped at the temporal position

optoacoustic qCWB peaks boost the loss saturation that develops the pulse-like fluctuations to the solitons. The SR is then much likely to be generated exclusively at the qCWB peaks. While the SRs have been regarded as irregular and hardly controllable in most cases, our observations suggest that we can engineer the SR emission by optoacoustically manipulating the qCWB landscape. To the best of our knowledge, this is the first experimental demonstration of control of the SRs by use of an intracavity source, rather than externally injected continuous-wave beams<sup>25</sup> or noise sources<sup>41</sup>.

Finally, in a similar fashion to the capturing of a single drifting pulse in Fig. 4a–c, the qCWB peaks can also catch and hold the SR. As shown in Fig. 5d, the SR emitted from a certain qCWB peak can be captured at the neighboring qCWB peak, where a secondary pulse bunch develops as the energy of the SR is accumulated there (see Supplementary Fig. 6 and Supplementary Movie 6 that correspond to Fig. 5d). This behavior of SR is more readily observed at the net cavity dispersions in the range of  $-7$  to  $-2 \text{ ps}^2 \text{ km}^{-1}$ , when their drift speed is small enough and the qCWB peaks are more apparent, as the case of trapping of a single drifting pulse in Fig. 4a–c. When the pulse bunch grows too

high as the SR is continuously absorbed, it is forcedly released and drifts toward the main mode-locked pulse bunch (Supplementary Fig. 7 and Supplementary Movie 7), and the overall process is repeated, a new secondary pulse bunch growing again at the same qCWB peak. On the other hand, when the drift speed of the SR is not sufficiently low, which is more likely to take place at larger values of  $|\beta_c|$ , the SR can be hardly trapped at the qCWB peak. Instead, the drift speed is temporarily reduced and recovered as the SR passes through the qCWB peak, and the SR collides eventually at the main mode-locked pulse bunch (see Supplementary Fig. 8 and Supplementary Movie 8 that show such a change in drift speed between 50 and 12 fs km<sup>-1</sup> at  $4\tau_T = 133$  ns). Our observations suggest the existence of the internal motions of the SR that have not been discovered yet, probably mediated by the ARs, besides the internal pulse bunching in the SR regime<sup>24</sup>.

## Discussion

It is worthwhile to discuss further the SR dynamics in Fig. 5d, Supplementary Fig. 6, and Supplementary Movie 6, where the SR generation lasts during a finite duration, as this SR type has not been reported yet. The generation and collision of the SR usually take place ceaselessly, as shown in Supplementary Figs. 3–5 and Supplementary Movies 3–5. In this case, the number of pulses in the main mode-locked pulse bunch is maintained to some extent through the balance between the absorption of newly arriving SR pulses and the disappearance of existing old ones in the main pulse bunch. In contrast, during the “temporary” SR process, the number of pulses in the main mode-locked pulse bunch increases, whereas the qCWB power is reduced. We explain the two distinct behaviors of SR states based on the slow EDF gain dynamics involving the gain competition between the main pulse bunch and the qCWB<sup>27,42</sup>. The main pulse bunch depletes the EDF gain more when it grows as absorbing the SR pulses, which reduces the gain that the qCWB experiences. The generation of the SR pulses also decreases the qCWB gain. When the qCWB gain falls significantly before a part of the main pulse bunch disappears, it becomes no longer sufficient to create more SR pulses, which eventually gives rise to the halt of SR generation (Supplementary Fig. 6 and Supplementary Movie 6). On the contrary, when the gain of the qCWB is still sufficient at the onset of the partial extinction of the main pulse bunch, the further suppression of the qCWB gain is prevented, which leads to the persistence of the SR generation.

Such gain dynamics can also explain a variety of more complicated forms of SR dynamics. We can also produce an SR state in which its generation stops and gets resumed repeatedly, as shown in Supplementary Fig. 9 and Supplementary Movie 9. Here, the initial SR created from the optoacoustic qCWB peak at  $3\tau_T = 100$  ns is merged to form a secondary pulse bunch, which depletes the EDF gain significantly. The qCWB gain then decreases, which stops the SR generation at the qCWB peak temporarily. The SR generation gets resumed after the secondary pulse bunch is eventually absorbed and subsequently a part of the main pulse bunch is annihilated so that the qCWB gain is recovered for the regeneration of optoacoustic qCWB peaks. The development of a secondary pulse bunch can also be seen when the SR generated from an optoacoustic qCWB peak is trapped and accumulated at the next neighboring one. The secondary pulse bunch can escape the optoacoustic qCWB peak when it grows too high so that the qCWB peak diminishes significantly due to the EDF gain depletion and cannot hold the secondary pulse bunch any longer via the XPM (Supplementary Fig. 7 and Supplementary Movie 7). When the secondary pulse bunch collides with the main one, the SR generation can get resumed in a similar fashion to Supplementary Fig. 9 and Supplementary Movie 9. We observe that the trapped pulse bunch is released when its energy gets close to that of the main pulse bunch,

as can be seen in Supplementary Fig. 7 and Supplementary Movie 7. For the rigorous theoretical analysis, however, it is necessary to take into account the complicated dynamical evolution of the qCWB and optoacoustic peaks via the slow EDF gain dynamics<sup>27,42</sup>. This is beyond the scope of this paper, and we leave it as future work.

We have reported the experimental demonstration of tailoring of nonequilibrium multi-pulse phenomena in a mode-locked fiber laser through optoacoustic manipulation of the qCWB landscape. The optically driven acoustic impulses that consist of the superposition of the simultaneously excited  $TR_{2m}$  ARs yield a set of impulsive qCWB fluctuations at specific temporal locations, which we could potentially adjust by changing the thickness of the AR-trapping optical fiber. The single-mode fiber cavity in which the cavity round-trip time is sufficiently longer than the AR decay time ( $\sim 100$  ns), and the optoacoustic effect is perturbative rather than dominant over the optical Kerr effect, is a unique, excellent platform for controlling and exploring a variety of MPD phenomena through optoacoustic manipulation of the qCWB. In particular, the NPR-based mode-locked laser cavity is advantageous for observation of various nonequilibrium MPD through the adjustment of intracavity PCs as well as pump power in a single experimental setup, thanks to the strong dependence of the intracavity nonlinear loss on the state of intracavity PCs. In this platform, we have experimentally shown that the optoacoustically induced impulsive qCWB fluctuations act as the point sources and attractive potentials for the bunched pulses and the SR. Hence, the optoacoustic qCWB fluctuations at the well-defined temporal positions offer a means to control the motion of a single drifting pulse or the emission and collision of SR, without complicated external injection of control signals into the laser cavity. Such controllability could be exploited to understand the SR dynamics further and unveil the mechanism of the SR generation that has not been clearly identified yet. Furthermore, while the amount of optoacoustic qCWB fluctuation is already sufficient to readily observe various types of MPD, we note that the strength of AR impulses could be enhanced coherently in the “resonance” condition<sup>18–20,23</sup> where the cavity round-trip time precisely matches an integer multiple of  $\tau_T = 33$  ns. This might provide further possibility to observe and control the optoacoustically manipulated MPD. Also, our observations provide new perspectives on studying ultrafast buildup of mode-locked pulses<sup>43,44</sup>, as they suggest the boost of the mode-locked pulse formation from the continuous-wave beats mediated by the ARs. In addition, in sharp contrast to most of the previous works where only the  $R_{0m}$  ARs were taken into account while the  $TR_{2m}$  ARs were neglected, we experimentally verify that the  $TR_{2m}$  ARs can play a critical role in mediating optoacoustically induced MPD phenomena. This might imply the existence of the undiscovered nature of optoacoustic interactions in mode-locked fiber lasers. Our work opens up new opportunities to extend the field patterning<sup>28,29</sup> to the qCWB and the navigation to more intriguing MPD in the mode-locked fiber lasers.

## Data availability

The data relevant to the plots within this paper are available from the corresponding author upon reasonable request.

Received: 21 May 2019; Accepted: 22 October 2019;

Published online: 11 November 2019

## References

1. Akhmediev, N. & Ankiewicz, A. *Dissipative Solitons* (Springer, 2005).
2. Grellu, P. & Akhmediev, N. Dissipative solitons for mode-locked lasers. *Nat. Photon.* **6**, 84–92 (2012).

3. Grudinin, A. B., Richardson, D. J. & Payne, D. N. Passive harmonic mode locking of a fibre soliton ring laser. *Electron. Lett.* **29**, 1860–1861 (1993).
4. Guy, M. J., Noske, D. U., Boskovic, A. & Taylor, J. R. Femtosecond soliton generation in a praseodymium fluoride fiber laser. *Opt. Lett.* **19**, 828–830 (1994).
5. Grudinin, A. B. & Gray, S. Passive harmonic mode locking in soliton fiber lasers. *J. Opt. Soc. Am. B* **14**, 144–154 (1997).
6. Malomed, B. A. Bound solitons in the nonlinear Schrödinger–Ginzburg–Landau equation. *Phys. Rev. A* **44**, 6954–6957 (1991).
7. Malomed, B. A. Bound states of envelope solitons. *Phys. Rev. E* **47**, 2874–2880 (1993).
8. Akhmediev, N. N., Ankiewicz, A. & Soto-Crespo, J. M. Multisoliton solutions of the complex Ginzburg–Landau equation. *Phys. Rev. Lett.* **79**, 4047–4051 (1997).
9. Afanasjev, V. V., Malomed, B. A. & Chu, P. L. Stability of bound states of pulses in the Ginzburg–Landau equations. *Phys. Rev. E* **56**, 6020–6025 (1997).
10. Richardson, D. J., Laming, R. I., Payne, D. N., Phillips, M. W. & Matsas, V. J. 320 fs soliton generation with passively mode-locked erbium fibre laser. *Electron. Lett.* **27**, 730–732 (1991).
11. Haboucha, A., Leblond, H., Salhi, M., Komarov, A. & Sanchez, F. Coherent soliton pattern formation in a fiber laser. *Opt. Lett.* **33**, 524–526 (2008).
12. Grellu, P. & Akhmediev, N. N. Group interactions of dissipative solitons in a laser cavity: the case of 2+1. *Opt. Exp.* **12**, 3184–3189 (2004).
13. Shelby, R. M., Levenson, M. D. & Bayer, P. W. Guided acoustic-wave Brillouin scattering. *Phys. Rev. B* **31**, 5244–5252 (1985).
14. Biryukov, A. S., Sukharev, M. E. & Dianov, E. M. Excitation of sound waves upon propagation of laser pulses in optical fibres. *Quant. Electron.* **32**, 765–775 (2002).
15. Dianov, E. M., Luchnikov, A. V., Pilipetskii, A. N. & Starodumov, A. N. Electrostriction mechanism of soliton interaction in optical fibers. *Opt. Lett.* **15**, 314–316 (1990).
16. Biryukov, A. S., Erokhin, S. V., Kushchenko, S. V. & Dianov, E. M. Electrostriction temporal shift of laser pulses in optical fibres. *Quant. Electron.* **34**, 1047–1053 (2004).
17. Jang, J. K., Erkintalo, M., Murdoch, S. G. & Coen, S. Ultraweak long-range interactions of solitons observed over astronomical distances. *Nat. Photon.* **7**, 657–663 (2013).
18. Kang, M. S., Joly, N. Y. & Russell, P. St. J. Passive mode-locking of fiber ring laser at the 337th harmonic using gigahertz acoustic core resonances. *Opt. Lett.* **38**, 561–563 (2013).
19. Stiller, B. & Sylvestre, T. Observation of acoustically induced modulation instability in a Brillouin photonic crystal fiber laser. *Opt. Lett.* **38**, 1570–1572 (2013).
20. Pang, M. et al. Stable subpicosecond soliton fiber laser passively mode-locked by gigahertz acoustic resonance in photonic crystal fiber core. *Optica* **2**, 339–342 (2015).
21. Pilipetskii, A. N., Golovchenko, E. A. & Menyuk, C. R. Acoustic effect in passively mode-locked fiber ring lasers. *Opt. Lett.* **20**, 907–909 (1995).
22. Erkintalo, M., Luo, K., Jang, J. K., Coen, S. & Murdoch, S. G. Bunching of temporal cavity solitons via forward Brillouin scattering. *New J. Phys.* **17**, 115009 (2015).
23. Pang, M., He, W., Jiang, X. & Russell, P. St. J. All-optical bit storage in a fibre laser by optomechanically bound states of solitons. *Nat. Photon.* **10**, 454–458 (2016).
24. Sugavanam, S., El-TaHER, A., Woodward, R., Kelleher, E. & Churkin, D. V. *Pulse Bunching In The Soliton Rain Regime Of An Ultralong Fiber Laser Mediated By Forward Brillouin Scattering*. CLEO/QELS FTu4A.4 (Optical Society of America, San Jose, 2016).
25. Chouli, S. & Grellu, P. Soliton rains in a fiber laser: an experimental study. *Phys. Rev. A* **81**, 063829 (2010).
26. Katz, M., Gat, O. & Fischer, B. Noise-induced oscillations in fluctuations of passively mode-locked pulses. *Opt. Lett.* **35**, 297–299 (2010).
27. Weill, R., Bekker, A., Smulakovskiy, V., Fischer, B. & Gat, O. Noise-mediated Casimir-like pulse interaction mechanism in lasers. *Optica* **3**, 189–192 (2016).
28. Leblond, H., Niang, A., Amrani, F., Salhi, M. & Sanchez, F. Motion of solitons of the complex Ginzburg–Landau equation: the effect of an external frequency-shifted source. *Phys. Rev. A* **88**, 033809 (2013).
29. Niang, A. et al. Harmonic mode-locking in a fiber laser through continuous external optical injection. *Opt. Commun.* **312**, 1–6 (2014).
30. Komarov, A., Komarov, K., Niang, A. & Sanchez, F. Nature of soliton interaction in fiber lasers with continuous external optical injection. *Phys. Rev. A* **89**, 013833 (2014).
31. Haus, H. A. & Mecozzi, A. Noise of mode-locked lasers. *IEEE J. Quant. Elect.* **29**, 983–996 (1993).
32. Kelly, S. M. J. Characteristic sideband instability of periodically amplified average soliton. *Electron. Lett.* **28**, 806–807 (1992).
33. Amrani, F., Salhi, M., Grellu, P., Leblond, H. & Sanchez, F. Universal soliton pattern formations in passively mode-locked fiber lasers. *Opt. Lett.* **36**, 1545–1547 (2011).
34. Santiago-Hernandez, H. et al. Dynamics of noise-like pulsing at sub-ns scale in a passively mode-locked fiber laser. *Opt. Exp.* **23**, 18840–18849 (2015).
35. Sakaguchi, H., Skryabin, D. V. & Malomed, B. A. Stationary and oscillatory bound states of dissipative solitons created by third-order dispersion. *Opt. Lett.* **43**, 2688–2691 (2018).
36. Le Quang, D., Jaouën, Y., Zimmerli, M., Gallion, P. & Thomine, J. B. Time-resolved measurement of dynamic frequency chirp due to electrostriction mechanism in optical fibers. *Photon. Technol. Lett.* **8**, 414–416 (1996).
37. Townsend, P. D., Poustie, A. J., Hardman, P. J. & Blow, K. J. Measurement of the refractive-index modulation generated by electrostriction-induced acoustic waves in optical fibers. *Opt. Lett.* **21**, 333–335 (1996).
38. du Mouza, L., Jaouën, Y. & Chabran, C. Transverse Brillouin effect characterization in optical fibers and its geometrical aspects. *IEEE Photon. Technol. Lett.* **10**, 1455–1457 (1998).
39. Diamandi, H. H., London, Y. & Zadok, A. Opto-mechanical inter-core cross-talk in multi-core fibers. *Optica* **4**, 289–297 (2017).
40. Singh, C. P. et al. Experimental study on soliton rain patterns in Yb-doped all-fiber standing wave cavity configuration. *Photon. Technol. Lett.* **28**, 1533–1536 (2016).
41. Schwartz, A. et al. *Formation, Sprinkling, Trapping And Annihilation Of Pulses In Passively Mode-locked Fiber Lasers With Modulated Noise*. CLEO/QELS JTU51 (Optical Society of America, San Jose, 2010).
42. Sulimany, K. et al. Bidirectional soliton rain dynamics induced by Casimir-like interactions in a graphene mode-locked fiber laser. *Phys. Rev. Lett.* **121**, 133902 (2018).
43. Ryczkowski, P. et al. Real-time full-field characterization of transient dissipative soliton dynamics in a mode-locked laser. *Nat. Photon.* **12**, 221–227 (2018).
44. Peng, J. et al. Real-time observation of dissipative soliton formation in nonlinear polarization rotation mode-locked fibre lasers. *Commun. Phys.* **1**, 20 (2018).

## Acknowledgements

We thank Mr. K. H. Nam for his technical support for preparation of the 2D viewgraphs in Supplementary Figs. 1–9. This work was supported by the National Research Foundation of Korea (NRF) grants funded by the Korea government (MSIT) (NRF-2016R1A2B4011862, NRF-2019R1H1A2079908).

## Author contributions

M.S.K. conceived and supervised the work. K.S.L. constructed the experimental setup and performed all the measurements. K.S.L., C.K.H., and K.J.M. analyzed the laser characteristics and multi-pulse dynamics. K.S.L. and D.S.H. analyzed the acoustic resonance modes and the in-fiber optoacoustic interactions. All authors had discussions and wrote the paper.

## Competing interests

The authors declare no competing interests.

## Additional information

Supplementary information is available for this paper at <https://doi.org/10.1038/s42005-019-0244-3>.

Correspondence and requests for materials should be addressed to M.S.K.

Reprints and permission information is available at <http://www.nature.com/reprints>

Publisher's note Springer Nature remains neutral with regard to jurisdictional claims in published maps and institutional affiliations.

 **Open Access** This article is licensed under a Creative Commons Attribution 4.0 International License, which permits use, sharing, adaptation, distribution and reproduction in any medium or format, as long as you give appropriate credit to the original author(s) and the source, provide a link to the Creative Commons license, and indicate if changes were made. The images or other third party material in this article are included in the article's Creative Commons license, unless indicated otherwise in a credit line to the material. If material is not included in the article's Creative Commons license and your intended use is not permitted by statutory regulation or exceeds the permitted use, you will need to obtain permission directly from the copyright holder. To view a copy of this license, visit <http://creativecommons.org/licenses/by/4.0/>.

© The Author(s) 2019